On the influence of mechanical loadings on the porosities of structural epoxy adhesives joints by means of in-situ X-ray microtomography

Vincent Dumont, Claudiu Badulescu, Georgios Stamoulis, Jérôme Adrien, E. Maire, Anthony Lefèvre, David Thevenet

On the influence of mechanical loadings on the porosities of structural epoxy adhesives joints by means of *in-situ* X-ray microtomography

V. Dumont[1,4,*], C. Badulescu[1], G. Stamoulis[3], J. Adrien[2], E. Maire[2], A. Lefèvre[4], D. Thévenet[1]

[1] ENSTA Bretagne, UMR CNRS 6027, IRDL, F-29200 Brest, France
[2] Univ. Lyon, INSA Lyon, UMR CNRS 5510, Laboratoire MATEIS, F-69621, Villeurbanne Cedex, France
[3] Univ. Bretagne Occidentale, UMR CNRS 6027, IRDL, F-29200 Brest, France
[4] Safran Reosc - Engineering & Integration Department - 91280 St Pierre-du-Perray, France

Keywords: Structural bonding, X-ray microtomography, Pores, Image processing
Corresponding author: vincent.dumont@ensta-bretagne.org

Abstract:
Structural bonding is a beneficial technique extensively used in numerous industrial fields. This technique is however prone to structural defects such as pores, which are created during the mixing of the adhesive and during the shaping of the joint. Depending on their characteristics, these pores are likely to influence the mechanical behaviour of adhesively bonded joints, as they induce local decreases in the cross-section of the bonds and they may also create threatening stress concentrations. It is also fair to assume that the characteristics of the pores within an adhesive joint are subject to changes when the assemblies are submitted to external loads. In order to investigate these changes, adhesively bonded samples were made using two different bicomponent epoxy structural adhesives. These samples were placed inside an X-ray tomograph, containing a tensile machine. *In-situ* X-ray tomography measurements were made simultaneously with the application of a tensile load on the samples. It was therefore possible to characterise the porosity states of each sample under mechanical loading, and to compute various quantities (porosity volumetric ratio, the pores number, equivalent diameters distributions, *etc.*). It was found that the pores in the joints are impacted by the increasing mechanical stress, resulting in pore nucleation, pore growth and coalescence. Moreover, the present study shows that this microstructural behaviour cannot be generalised, as different adhesives may display different properties.

1. Introduction

A wide range of industrial fields nowadays use structural bonding for their applications, such as aeronautics, automotive or renewable energies. This extensive use is explained by the many advantages adhesive bonding features as opposed to bolting or riveting: multimaterials assembly capabilities, decrease in weight, preserved structure integrity, *etc.* Unfortunately, this technique also has disadvantages [1]: the quality of the bond highly depends on the bonding process (surface treatment, curing, *etc.*) [2], the mechanical behaviour of structural adhesives is non-linear and difficult to model accurately, and bonding defects are very likely to happen during the shaping of the joint. These imperfections, often unavoidable, include the presence of pores within the material. These pores, created during the mixing of the adhesive components and during the shaping of the adhesive joint, can be a threat to the good mechanical strength of the bond: they damage the integrity of the material, they decrease the cross-section of the joint, and they can induce unwanted stress concentrations. These pores being structural defects inside the adhesive joint, it is fair to hypothesise that they could have an influence on the mechanical properties of a bonded assembly. To validate this assertion, it is however essential to be able to detect these pores inside an adhesive joint.

X-ray microtomography is a fairly popular solution to detect and visualise such entities located in a bulk of a medium. This technique is increasingly used in materials science due to its various advantages as it is detailed by Buffière *et al.* [3]: it is non-destructive, the measurements are three-dimensional, it allows the visualisation of the internal structure of non-transparent media, *etc.* Moreover, depending on the tomograph, the resolution of the measurements can be lesser than 1 µm, which is a quite attractive feature for damage and defects detection. That is why this tool has been used in the past on a variety of materials for similar purposes such as alloyed metals and composite materials. For instance, Liu and Bathias studied the effects of the presence of pores in a Aluminium alloy reinforced composite in terms of tensile and fatigue properties [4]. In a similar fashion, Breunig *et al.* managed to detect fibre fracture and interface debonding in a SiC/Al MMC material under wedge and 3-points bending loadings using X-ray tomography [5]. Polymeric materials were also

studied using such a technique: in particular Garcea *et al.* succeeded in visualising cracks in a polymer composite [6], in spite of the many experimental issues specific to X-ray measurements performed on these materials. Notably, the authors used the reconstructed volumes to build a Finite Element Model, so as to be able to predict both damage initiation and propagation in the material. As far as damage characterisation is concerned, *in-situ* microtomography measurements are particularly useful, as they enable the tracking of both the appearance and the evolution of damage-related phenomena under mechanical stress (crack propagation, pores coalescence, delamination, *etc.*), as shown in numerous studies carried on by the teams of Maire, Adrien and Buffière [7]–[11]. Most of these reference works take advantage of *in-situ* X-ray tomography to characterise materials under various types of loadings: metals under tensile loading [10], polymeric syntactic foams under compression [11], metal matrix composites loaded in tension [8], *etc.*

On the subject of polymers, a few studies may be found in the literature. A commonly found topic is the fabrication of polymeric structures by means of additive manufacturing processes. These techniques tend to generate voids in the resulting materials, which are easily studied using X-ray microtomography. For instance, a paper released by Pavan *et al.* in 2016 characterised the porous network of laser-sintered polyamide structures, for different sizes [12]. It was found that the size of the structure had a significant influence the characteristics of the voids created during the process. More recently, Wang *et al.* proposed a micromechanical model in order to characterise the mechanical behaviour of 3D-printed polymers [13]. Nonetheless, few studies may be found specifically on adhesives, and even more so regarding adhesively bonded assemblies. This is probably explained by the *a priori* low risk of pore creation for these materials when compared to additive manufactured polymers. X-ray tomography has been fairly recently applied to the field of structural bonding, but mainly to characterise the interfaces between adhesives and adherend. For example, Schwarzkopf [14] used tomography measurements coupled with simulations to build a micromechanical model of adhesive-wood interfaces. McKinley *et al.* [15] took advantage of this experimental technique to characterise the bonding process and the penetration of the adhesive in the fibrous structure of wooden pieces. Virtually no attention has been given to the precise study of the microstructure of adhesive joints, whereas it may be an important factor to describe macroscopic phenomena, such as crack propagation. It should however be reminded that microtomography is not the only experimental technique able to quantify the porous state of polymers, or materials in general. For instance, one can use gas sorption and Hg injection, as it has been done by Rohr *et al.* [16] for porous resins derived from acrylate monomers. Such techniques are able to provide valuable data for extremely small pores, which cannot be visualised through X-ray tomography. However, it should be noted that less extensive knowledge regarding the geometry of the pores is obtained using these techniques, and they may not be suited to the study of bonded assemblies for *in-situ* testings, for example.

In this paper, the authors characterise the effect of an out-of-plane tension stress on the detectable pores included in adhesives joints using *in-situ* X-ray microtomography measurements. This is achieved on bonded assemblies, using two bicomponent epoxy adhesives. This characterisation is performed for various values of the applied load, in order to track diverse porosity-related quantities, such as the number, the volumetric fraction, the diameters distribution *etc.* A discussion on the results is finally proposed, so as to explain the highlighted phenomena. It should be reminded that this aim of this study is not the absolute characterisation of the porous network of these materials, but the detection of phenomena achievable with state-of-the-art laboratory tomography on adhesively bonded assemblies.

2. Preparation of the samples

2.1. Design

The samples used in this study are butt-joint samples, bonded using a structural bicomponent epoxy adhesive. The dimensions of the samples are kept relatively small, in order to fit in the tomograph used for the tests campaign. As such, they are designed to feature a 6x6 mm^2 bonded surface (Figure 1a). These samples are waterjet cut from Aluminium 2017A Scarf samples to form a rake-shaped pattern as shown in Figure 1b. Each specimen is then to be cut from its Scarf base after the curing (Figure 1c), as it is detailed further.

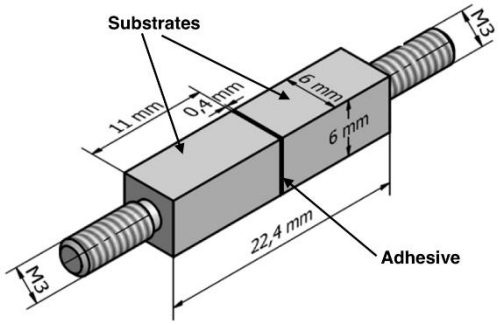

(a) *In-situ* microtomography tensile samples geometry

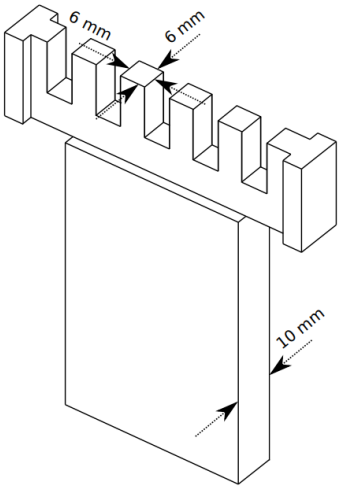

(b) Samples cutting pattern on a Scarf geometry

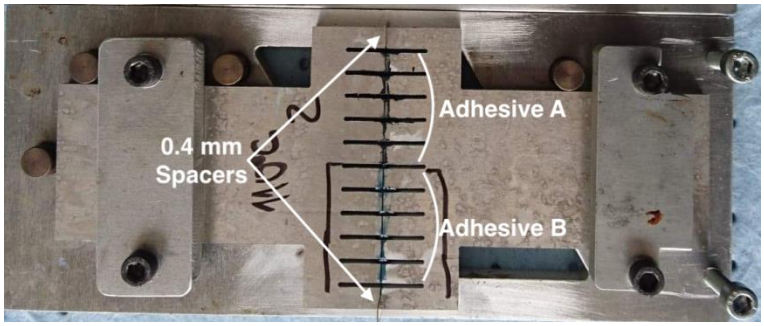

(c) Bonded modified Scarf samples

Figure 1 : Modification of SCARF geometries for in-situ tomography applications

2.2. Bonding and curing

A standard surface treatment procedure is applied to the samples to obtain good adhesion conditions. This treatment sequentially includes acetone degreasing, grinding with grade 180 sandpaper, and a final acetone cleaning. These steps ensure the removal of any oily impurities and oxide layers which could have been formed during the machining, the storage and the handling of the substrates.

As it has been stated in the introduction section, the study is performed on two different bicomponent epoxy adhesives (adhesive A and adhesive B). Adhesive B to the *Huntsman™ Araldite 420* adhesive. The trade name of adhesive A cannot be communicated for reasons of confidentiality. A few general properties are given in **Erreur ! Source du renvoi introuvable.**. These adhesives have similar curing properties in terms of duration and temperature, according to the datasheets provided by the manufacturers and to Differential Scanning Calorimetry (DSC) measurements. The mixing of the components is performed with a planetary mixing device (1500 rpm for 7 minutes) in order to guarantee homogeneity.

Property	**Adhesive A**	**Adhesive B**
Texture	paste-like	paste-like
Known fillers	-	glass beads
Glass transition temperature (DSC)	~ 90°C	~ 60°C
Young's modulus [MPa]	1400	2000
Poisson ratio [-]	0.33	0.41

Table 1 : A few properties for the considered adhesives

The *Huntsman™ Araldite 420* is an epoxy-based adhesive with a bisphenol A diglycidyl-ether prepolymer and a diamine hardener mixed in stoichiometric conditions. The adhesive A is also an epoxy-based adhesive, with a bisphenol A epichlorohydrin prepolymer, and a titanium dioxide charged propylamine hardener.
The adhesives were spread on the bonded surfaces using a stainless steel spatula, and the two Scarf substrates are then assembled together (Figure 1c) with a specially designed setup. The role of this setup is to control both the alignment of the substrates and the thickness of the adhesive joint. In this work, the thickness is set to 0.4 mm, using calibrated spacers (Figure 1c).
The Scarf assemblies are then put inside a *Memmert UF110+™* thermal chamber to be cured (1h10 at 110°C). DSC tests were performed on the adhesives thusly cured, to check that the polymerisation rates were above 95% (*i.e.* that the adhesives can be considered to be fully polymerised).
Finally, the microtomography samples (Figure 1a) were waterjet cut from their Scarf base (Figure 1b), and threaded holes are machined at each end so as to apply a mechanical load.

3. Experimental method

3.1. X-ray tomography principle

The interested reader may find detailed information on this particular matter in [17].
Microtomography is a non-destructive, three-dimensional imaging technology originally developed and used for medical applications [3], [18]. As such, it quickly became of interest for materials science, as it allows researchers to access data from the bulk of a non-transparent material. Moreover, these data are three-dimensional, with a resolution down to 1 µm per pixel [3].
The technique relies upon the variation of the X-ray attenuation phenomenon within an inhomogeneous material, when crossed by X-ray beams. This variation, closely linked to the internal structure of the medium, can be used to reconstruct the complete volume of the observed sample. To do so, the investigated volume is exposed to X-rays along various propagation paths using different angular positions (Figure 2). The gathered data from the X-ray detector (Figure 2) for each of these paths allow for the reconstruction of the complete volume by means of a reconstruction algorithm, provided by the manufacturer of the tomograph. More information about the possible reconstruction techniques may be found in [17]. The reconstruction step allows for the visualisation of the map of the linear attenuation coefficient$\mu(x, y, z)$, which results from the X-ray attenuation phenomenon within the material. This coefficient being inherently linked to the medium structure, the spatial map of $\mu(x, y, z)$ is equivalent to the spatial reconstruction of the medium microstructure.

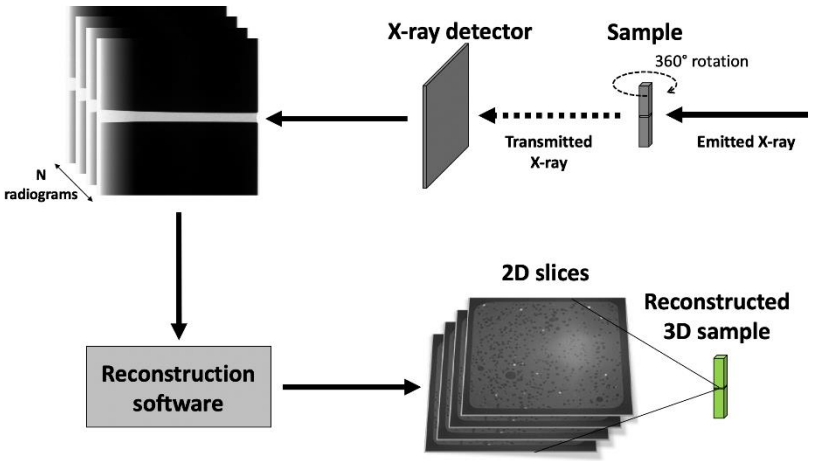

Figure 2 : Tomography measurements principle

In the following paper, it is assumed that this technique is reliable enough to give an accurate description of the microstructure of the investigated joints. This is moreover validated by comparing

the dimensions of substrates measured by an optical microscope on one hand and by the tomograph on the other hand. A gap lesser than 0.15% was found.

3.2. Test procedure

The tomograph used in the following study is a *Phoenix*^{TM} *VtomeX* equipped with a 1920x1536 pixels *Varian Paxscan*^{TM} X-ray detector. The chamber of this tomograph includes a 3kN electromechanical tensile machine to perform *in-situ* measurements as shown in Figure 3. The radiograms (Figure 2) delivered by the detector are 16-bits greyscale pictures, to be used by the reconstruction software to build the 3D volume of the investigated sample. The measurements are performed with a voxel size of 4.5 µm x 4.5 µm x 4.5 µm, which is the best achievable resolution with respect to the dimensions of the samples. As it is shown in Figure 2, attenuation data for several propagation paths (*i.e.* several angular positions of the sample with respect to the X-ray beam) are needed. For these measurements, 1200 radiographs were recorded during the 360° rotation (Figure 2) with an exposure time of 500 ms each, resulting in an acquisition time of roughly 10 minutes. The X-ray source was operated with a voltage of 80 kV and a current of 280 µA.

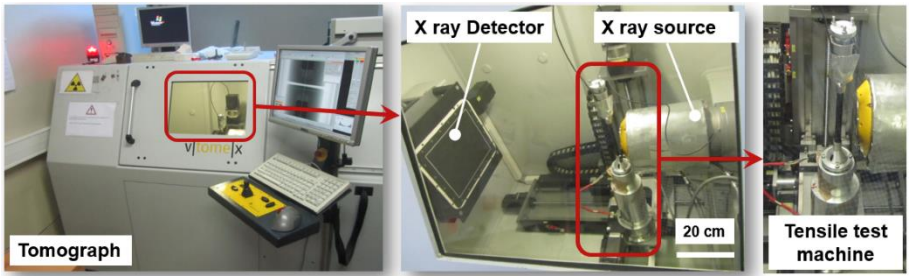

Figure 3 : Experimental set-up

This was performed for various tensile loads in order to investigate the influence of the application of a mechanical stress to the detected pores in the adhesive joints. During the acquisition time, the displacement of the moving part of the tensile machine was stopped (Figure 4). The displacement was then increased to proceed to the next step, with a rate of 0.4 mm.min^{-1}. This process was continued until the failure of the sample. The resulting load on the samples is shown in Figure 5. It is clear that the load is evolving for each step, especially for the higher levels, due to stress relaxation mechanisms. In order to reduce the influence of this phenomenon on the measurements, a stabilisation time is kept before launching the acquisition.

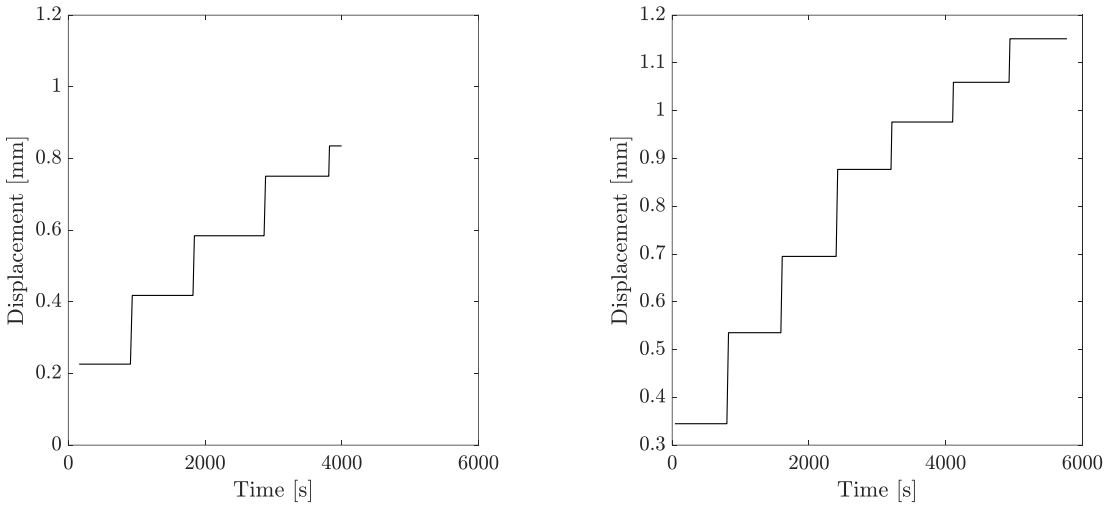

(a) Adhesive A (b) Adhesive B

Figure 4: Displacement steps applied to the samples

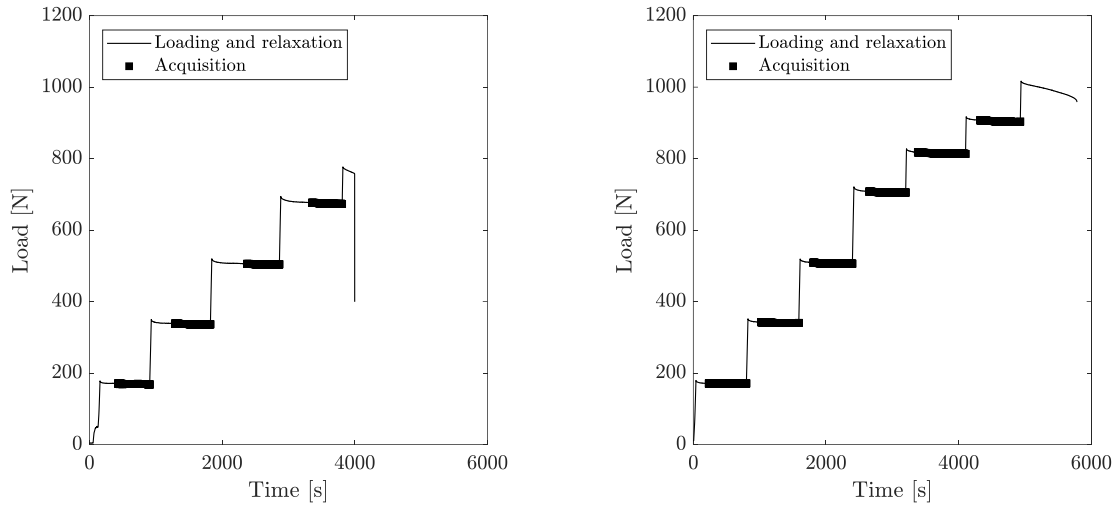

(a) Adhesive A (b) Adhesive B

Figure 5: Resulting load on the samples

3.3. Tomographic data processing

The main challenge is to isolate the different phases in the reconstructed volumes: the air in the pores, the adhesive, and the aluminium substrates. If the adhesive contains glass beads or other mineral charges, such as the adhesive B, they are included in the substrates phase, for they appear at similar greyscale levels. This step, known as segmentation, is very common in image processing and a large number of methodologies has been suggested to segment greyscale or colour data.

An easy approach is to use one or several thresholds depending on the number of phases to be segmented. These thresholds divide the pixels in the data depending on their greyscale level, to form the desired phases. The value of the thresholds can be chosen, or preferably computed by means of various algorithms [19].

Other methodologies, which do not rely on thresholds, also exist. Among these, the watershed algorithm [20] was successfully applied to image segmentation [21]. Another popular approach is to use region growing algorithms [22], adapted from the random walker probabilistic model [23]. Due to the shape of the histogram of the reconstructed volumes (Figure 6), a threshold-based method is chosen: the three phases within the material are well-defined (see the peaks on the histogram in Figure 6).

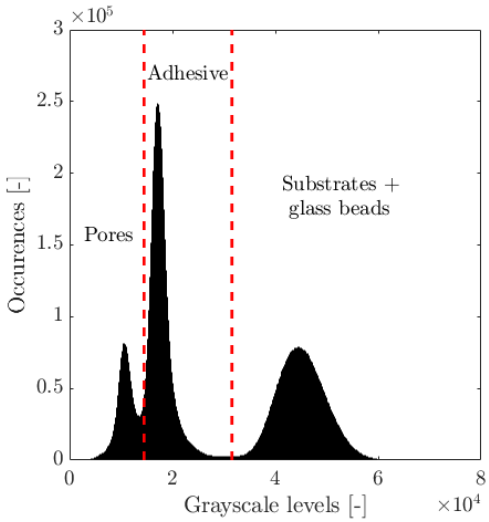

Figure 6: Histogram of a reconstructed volume and thresholds computed using Otsu's method

The thresholds are calculated using Otsu's method [24]. This method optimises the thresholds values so as to obtain maximal inter-phase variance in terms of pixels greyscale levels. Firstly introduced for the calculation of one threshold to segment bimodal data, it may also be generalised to a greater number of thresholds [24]. In the scope of this study, two thresholds are needed (*i.e.* multithresholding), in order to segment trimodal data (Figure 6). Thresholding is however sensitive to measurement noise; that is why a contour-preserving [25] three-dimensional median filter is previously applied to reduce this disturbance. The kernel size of this filter is set to 5 voxels. As a result, all the segmented objects whose size is lesser than that of the kernel of this filter were removed (which roughly corresponds to a 22 µm pore diameter, since too high of an uncertainty impacts their segmentation).
The volumes are then segmented using the computed thresholds, resulting in the data shown in slices to Figure 7.

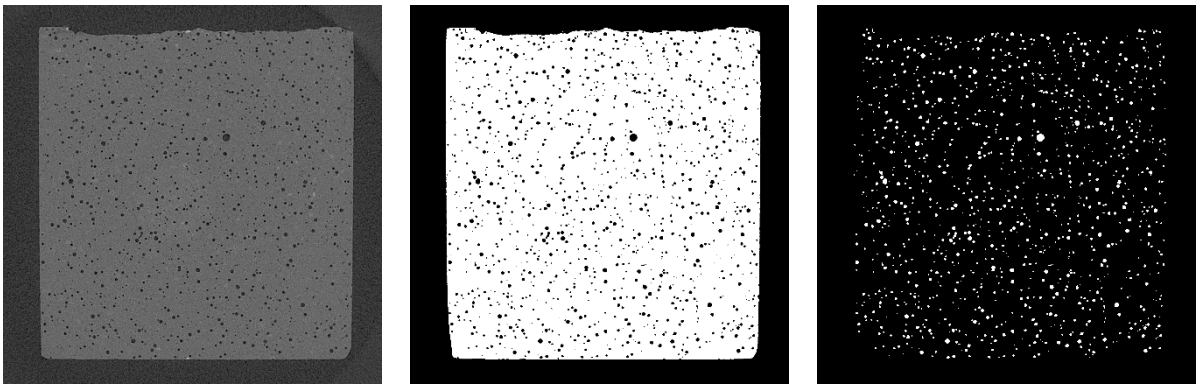

(a) Raw data (b) Adhesive (white pixels) (c) Pores (white pixels)

Figure 7: Data segmentation output (Adhesive A, initial state, sliced halfway through the joint thickness)

The segmented volumes are then screened to remove segmentation errors or unwanted objects (*i.e.* pores whose volumes are lower than the median filter kernel size, for instance). Finally, connected components analysis can be performed on these screened volumes to obtain various geometrical and statistical quantities.
In order to investigate the influence of the measurement noise on the segmentation, artificial tomographic results were generated, in such a way they resemble the experimental volumes as well as it is possible at this stage of the study, in terms of greyscale levels, noise, and pores sizes. In particular, the experimental noise was estimated by subtracting two microtomographic acquisitions of the same volume. The standard deviation of the resulting greyscale levels was then used to generate an artificial Gaussian noise, to be applied on the synthetic volumes. The tool was then applied to these artificial datasets, and the detected pores numbers and pores volumetric ratios were compared to the values imposed during the creation of the artificial data. The results are presented in Figure 8.
From these data, one may notice that the error committed during the segmentation can be divided into two separate parts: a systematic error (*i.e.* a global offset from the reference values) and a punctual error, resulting in fluctuations around a mean value (Figure 8c and Figure 8d).

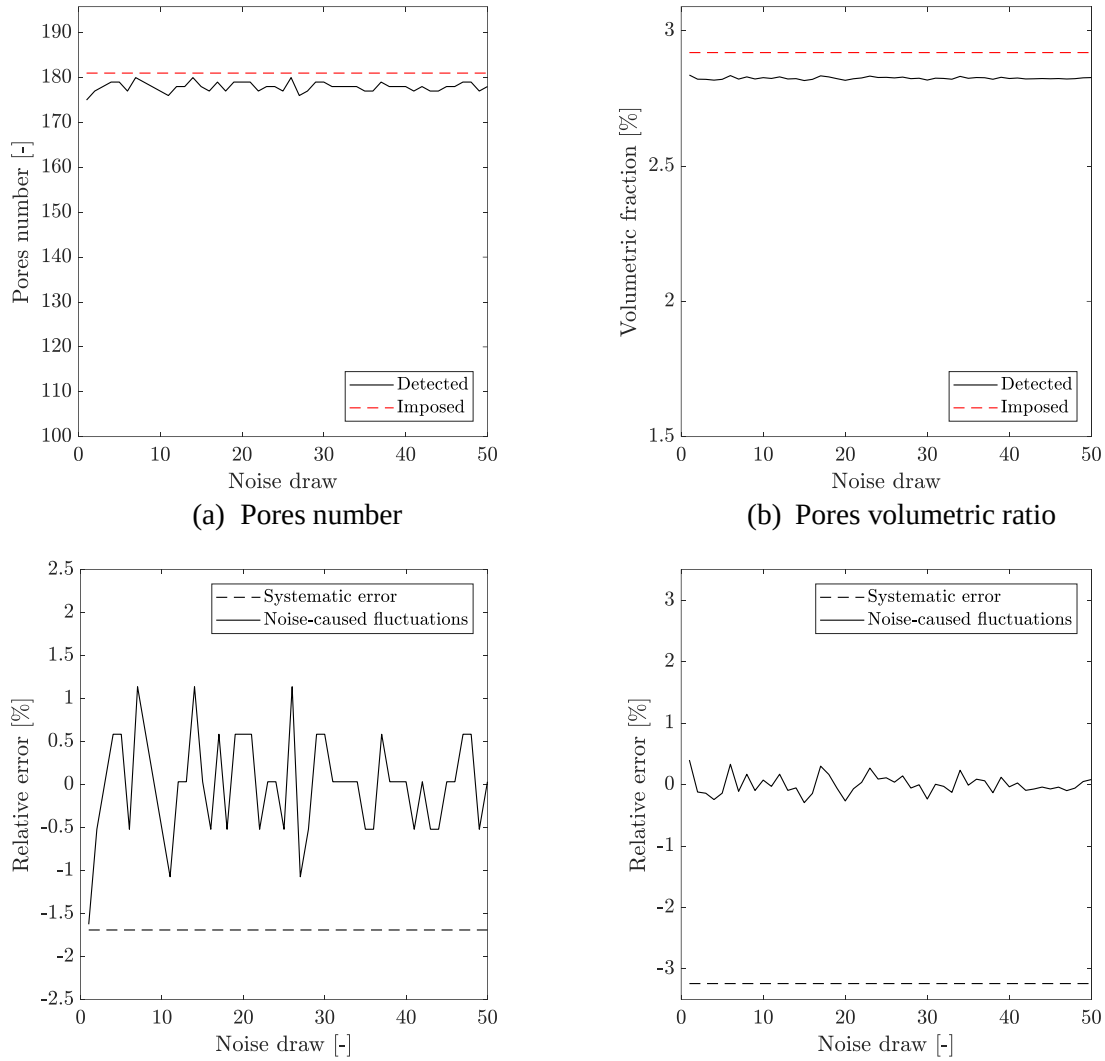

(a) Pores number (b) Pores volumetric ratio

(c) Pores number (d) Pores volumetric ratio

Figure 8: Comparison between imposed and detected properties for various noise draws in a synthetic dataset

The systematic error is expected to be a consequence of the processing method itself. Since the pores from one load step to another are subjected to minor changes, this component of the error should lead to an offset between the actual experimental values and the detected experimental values, fairly independent of the applied load. On the other hand, the measurement noise varies from one load step to the next, and therefore may have a quantifiable influence on the results, mostly in terms of uncertainty on the detected quantities. This influence may be estimated using the standard deviation of the detected data in Figure 8a and Figure 8b. More precisely, it is possible to compute a relative error for each noise draw in Figure 8a and Figure 8b, and to extrapolate these error values and their statistics to the experimental data, so as to estimate the uncertainty on the detected results.

4. Results

4.1. Porosity volumetric ratio and number of pores

As these tomographic measurements were performed for various loads applied to the samples, it is possible to apply the analysis technique presented above to each dataset, in order to track the evolution of some characteristics that may be extracted from the segmented volumes. In a first stage, the following quantities shall be investigated: the porosity ratio η (Equation 1), and the number of pores in the adhesive joints.

$$\eta \;=\; 100 * \frac{V_{por}}{\sum_{i \in phases} V_i}$$

Equation 1

where V_{por} is the volume of the pores and V_i is the volume of the phase i.

Three-dimensional views of the detected pores in each adhesive joint (in their initial state) can be found in Figure 9. An immediate observation that can be made is that the pores properties depend on the adhesive, since the segmentation yields very different results between adhesives A and B.

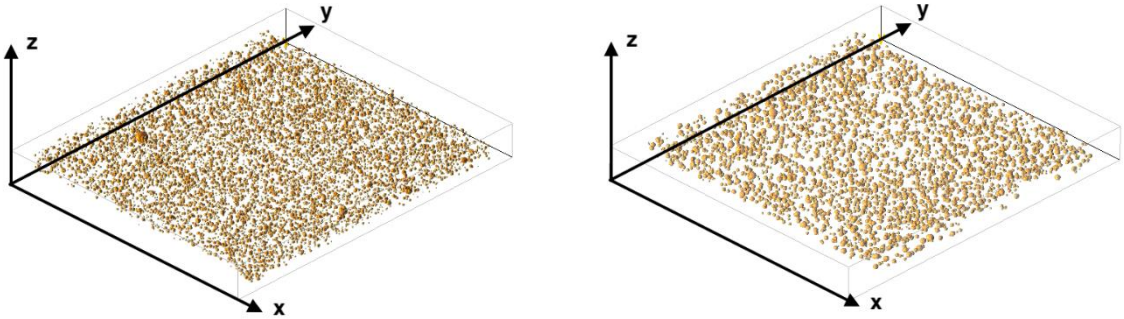

(a) Adhesive A (b) Adhesive B

Figure 9: 3D view of the pores in the adhesive joints

These quantities are computed for each load step, and the results are given in Figure 10 and Figure 11. It should be noted that the porosity volumic fraction presented in Equation 1 is expressed as percentages in Figure 11. The data in Figure 10 and Figure 11 feature error bars estimating the uncertainty caused by the experimental noise. These error bars were computed using the relative errors displayed in Figure 8c and Figure 8d. It should also be noted that the error bars in Figure 11b are plotted but almost undistinguishable from the data.

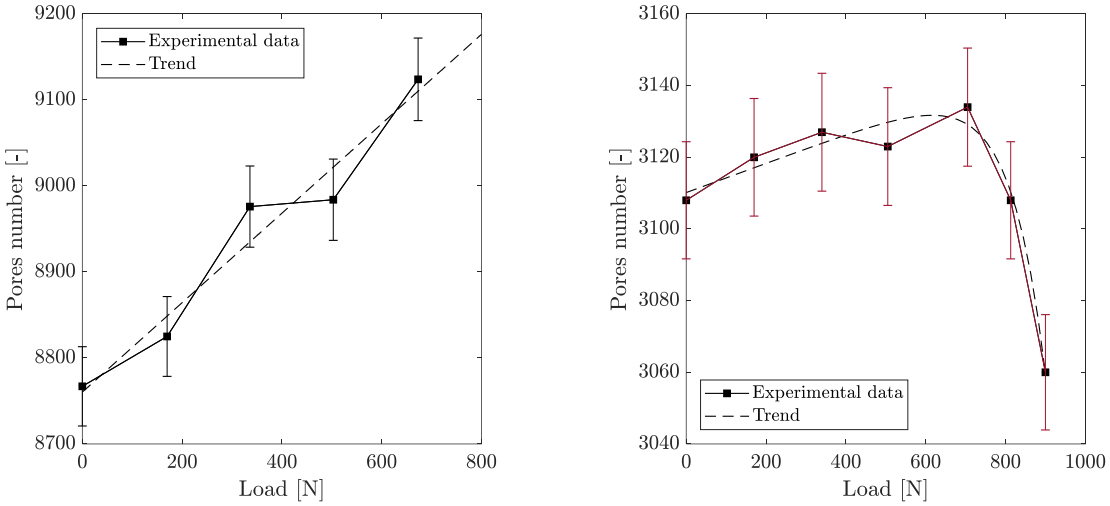

(a) Adhesive A (b) Adhesive B

Figure 10: Number of pores detected in the adhesive A and the adhesive B versus the applied load

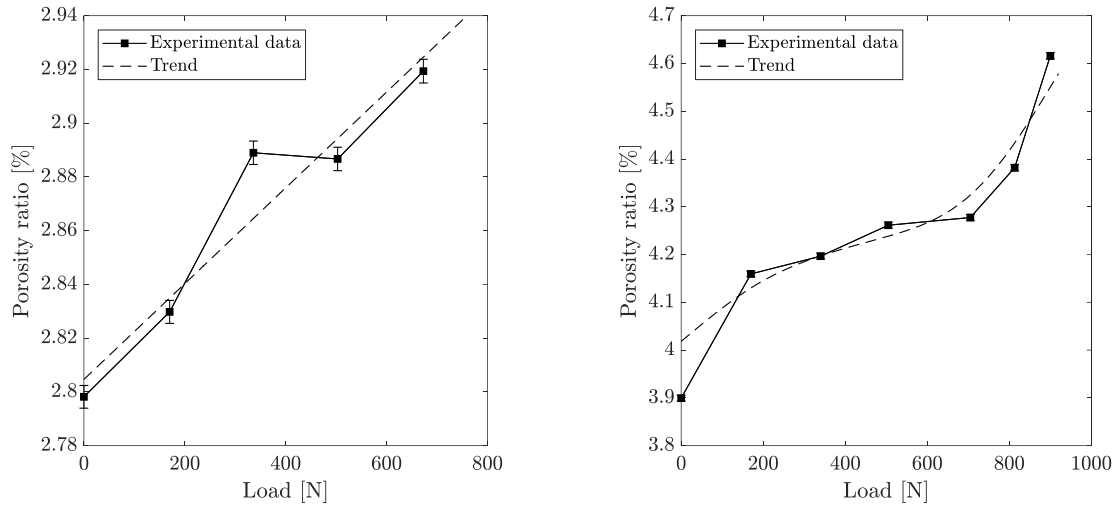

(a) Adhesive A (b) Adhesive B

Figure 11: Porosity ratios in the adhesive A and the adhesive B versus the applied load

It appears from Figure 10 that the two adhesives exhibit very different behaviours when the joint is mechanically stressed. The adhesive A shows an ever-increasing number of pores, which tends to suggest that voids nucleate all along the experiment. On the contrary, the behaviour of the adhesive B may be divided into two successive regimes. At first, the number of detected pores slowly increases, similarly to the behaviour of the adhesive A, until a critical load value F_{cr} (approximately 700 N). Once this critical value is reached, there is an abrupt decrease in the number of pores from this F_{cr} value to the failure of the sample, which is typical of pores coalescence. Those two domains seem to be linear with respect to the applied load, as is the behaviour shown by the adhesive A. One may also notice that the adhesive A contains significantly more air voids than the adhesive B (Figure 10, roughly between 2.8 to 3 more pores in the adhesive A than in the adhesive B).

This piecewise definition is also valid for the porosity ratio in the adhesive B when it is plotted versus the applied load (Figure 11). The transition between the first and the second regime for the porosity ratio occurs at the same F_{cr} as for the pores number. However, contrary to what could be expected from the data presented in Figure 10, the second regime for the porosity ratio consists of a steeper increase of this quantity. Even though this observation may seem paradoxical in a first stage, it could also be the appearance of a coalescence phenomenon, meaning that the pores are merging, rather than disappearing. This coalescence phenomenon has been widely observed and studied for various materials [26]–[28]. One may visualise this phenomenon, coupled with pore growth, on the CT-scans images, located in various sites. Once the segmentation is performed, it is possible to build the 3D geometry of the pores from the binary segmented volumes, and one may clearly see that the coalescence of the relevant pores has been correctly detected. One can also notice in Figure 12a and Figure 12b that in addition to the merging of the voids, the pores undergo an increase in volume and tend to expand. New pores also opened, through nucleation phenomena (Figure 12b).

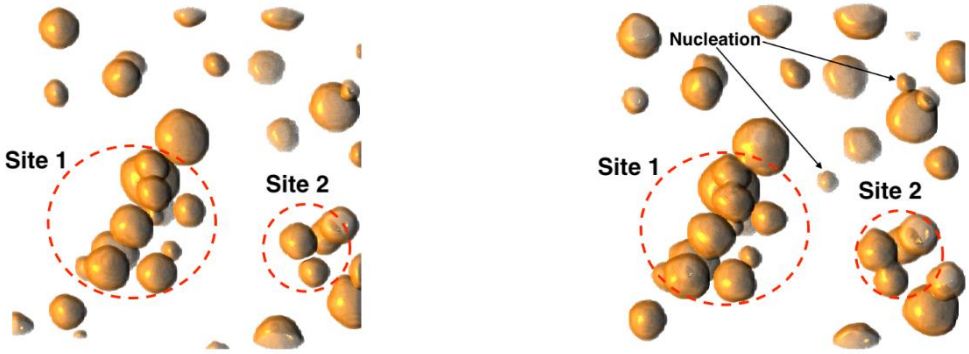

(a) Coalescence sites, adhesive B, 0 N (b) Coalescence sites, adhesive B, 900 N

Figure 12: Coalescence sites visualised for two different load levels, adhesive B

Even though an influence of the applied load is detected using the segmentation tool, little to no changes can be pinpointed visually on the reconstructed volumes, as it is shown in Figure 13. This is due to the fact the changes undergone by the material from the initial to the final state of the experiments are very tenuous. For most cases, these changes correspond to differences of a few pixels, which makes them difficult to visualise.

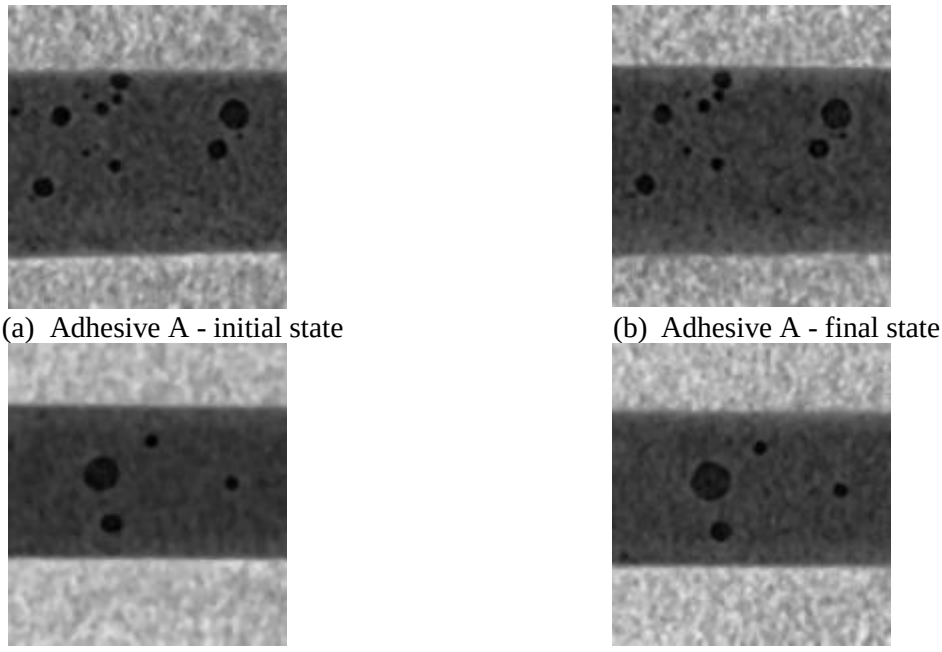

(a) Adhesive A - initial state (b) Adhesive A - final state

(c) Adhesive B - initial state (d) Adhesive B - final state

Figure 13: Reconstructed volumes sliced in the middle of the bonded surface

4.2. Equivalent diameters distributions

The apparent absence of coalescence for the adhesive A could be explained by the very different characteristics of the corresponding detected pores field. This difference may be highlighted by the comparison of the distribution of the equivalent diameters of the voids, as already suggested for the comparisons in the initial state (see Figure 14a and Figure 14b). The equivalent diameter of an object is defined as the diameter of the sphere featuring the same volume.

It is obvious from Figure 14a that the large majority of the pores in the adhesive A are rather small (the average diameter being of approximately 36 µm), while the average diameter for the adhesive B is roughly 1.6 times greater (~57 µm, Figure 14c and Figure 14d). Due to the limitations in terms of measurement resolution, and given the shape of the distribution presented in Figure 14a, one could

possibly conclude that there are some data and phenomena related to adhesive A that cannot be detected in this test configuration. The shape of the diameters distribution given in Figure 14a suggests that there is a fair number of pores whose diameters are lesser than 20 µm going undetected.

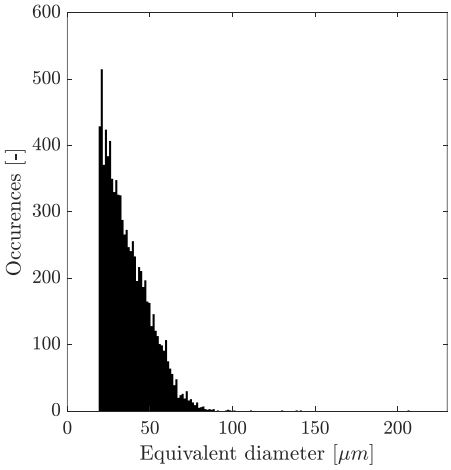

(a) Diameters distribution for the adhesive A, 0 N

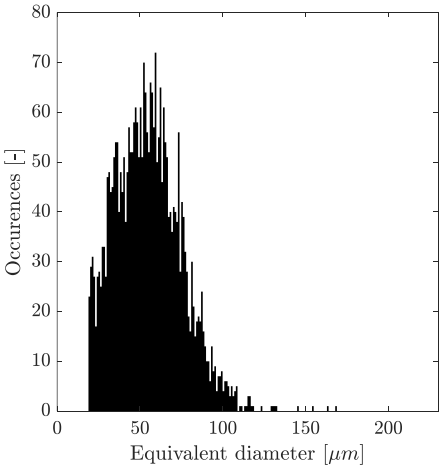

(b) Diameters distribution for the adhesive A, 0 N

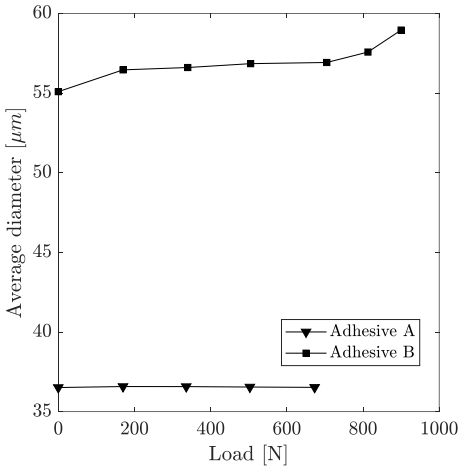

(c) Evolution of the average diameter with the applied load

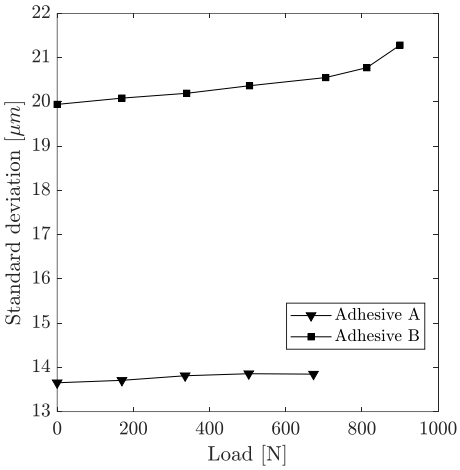

(d) Evolution of the standard deviation with the applied load

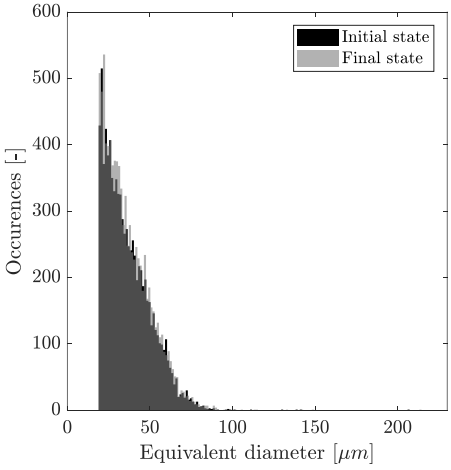

(e) Initial and final diameters distributions, adhesive A

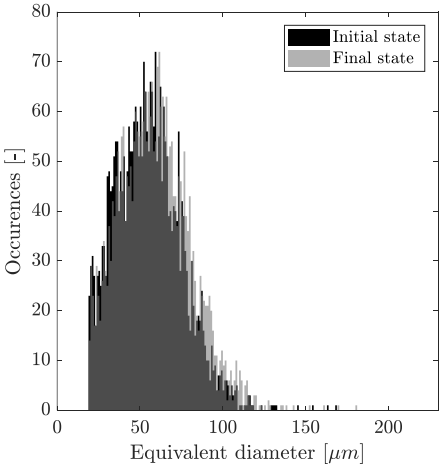

(f) Initial and final diameters distributions, adhesive B

Figure 14: Comparison of the diameters distributions and evolution of their statistics

It is worth noticing that the fluctuations of the statistics of the distribution for the adhesive A are one order of magnitude lower than those for the adhesive B (Figure 14c and Figure 14d), and therefore should be pondered with respect to the resolution of the measurements. One possible conclusion would be that very few changes of the microstructure are occurring for the adhesive A. This could be confirmed by Figure 14e, which shows seemingly identical distributions, contrary to Figure 14f, for which a slight offset towards the increasing diameters is observed. This corresponds to the increase of the average diameter shown in Figure 14d and visible in Figure 12.

4.3. Pores shape

The extracted pores seem to be spherical in all the investigated cases, as it is suggested by Figure 12. It is possible to quantify this roundness, for each individual, by computing its sphericity Ψ as shown by Wadell [29]. This quantity, defined by Equation 2, is useful to characterise the similarity between a particle of volume V_p and of area A_p, and a sphere.

$$\Psi = \frac{\pi^{\frac{1}{3}}(6V_p)^{\frac{2}{3}}}{A_p}$$

Equation 2

Thanks to connected components analysis, it is easy, for each segmented porosity, to access its volume and its area, and therefore to compute Ψ. This allows to track the possible variations in shape that may occur during the application of a mechanical load. The corresponding data is displayed in Figure 15.

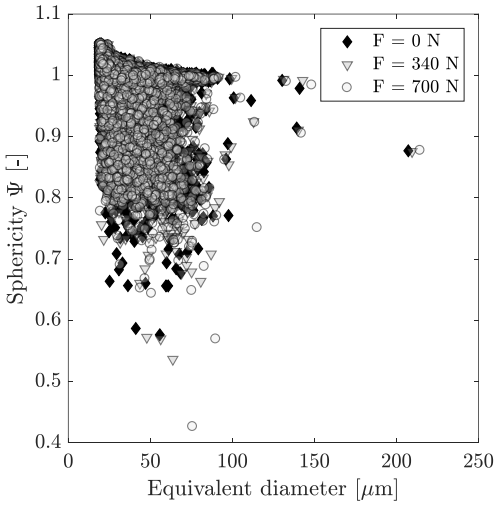

(a) Sphericity of each porosity versus its equivalent diameter for various loads (adhesive A)

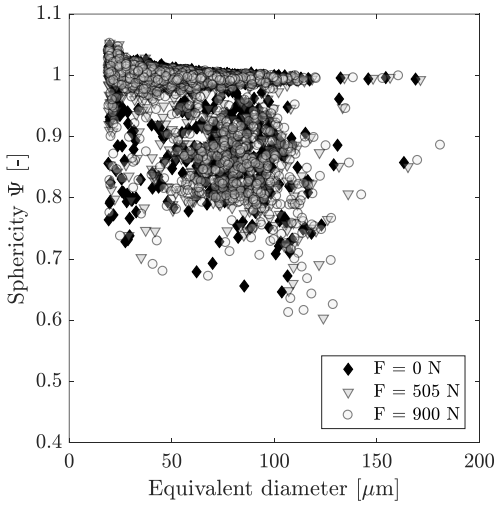

(b) Sphericity of each porosity versus its equivalent diameter for various loads (adhesive B)

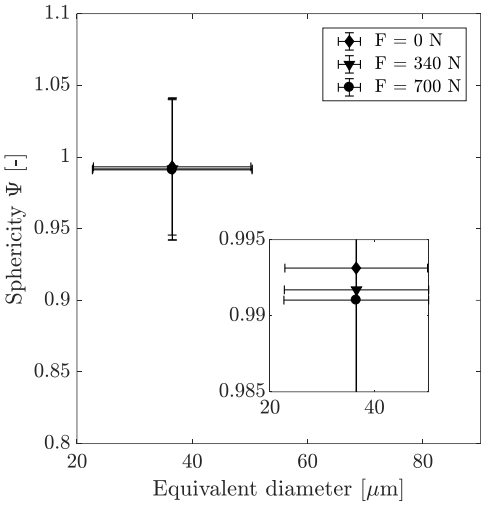

(c) Evolution of the average point (adhesive A)

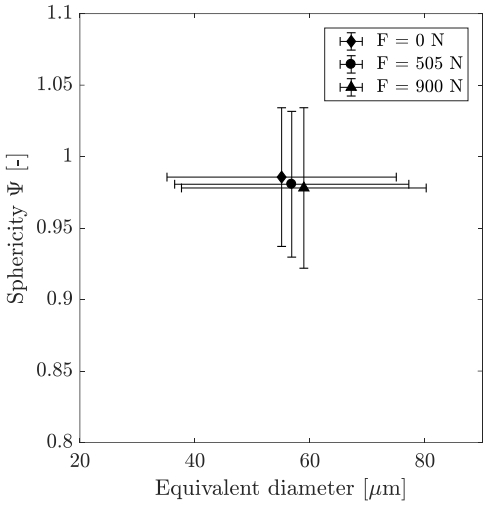

(d) Evolution of the average point (adhesive B)

Figure 15: Influence of a mechanical load on the sphericities of the pores

From the data in Figure 15a and Figure 15b, it is clear, as it was assumed, that the large majority of the pores, are quasi-spherical for both adhesives. One may also spot a few values greater than 1, especially for small equivalent diameters, which is seemingly paradoxical. This is due to the effect of voxelisation which can lead to slightly erroneous areas calculations, as it is explained in [30].

Even if the data provided in Figure 15a and Figure 15b are very exhaustive and give a good visualisation of the pores shapes for a given load state, due to the large amount of points it is difficult to extract a trend from one point cloud to another. In order to do so, it was chosen to compute the average point for each point cloud, as shown in Figure 15c and Figure 15d. These average points are simply located at the coordinates (μ_d, μ_Ψ), μ_d being the mean of the equivalent diameters and μ_Ψ being the mean of the sphericity values. The error bars on these figures are calculated using the standard deviations of the equivalent diameters and the sphericities respectively. These graphs highlight the shift occurring towards the decreasing sphericities, especially in the case of the adhesive B (Figure 15d). This result seems consistent with the application of a mechanical load, as the initially spherical pores (due to the surface tension) are slightly deformed into ovoids due to the normal stress applied to the adhesive joints.

This leads to the conclusion that the geometrical transformations undergone by the pores within an adhesive joint under mechanical loading are strongly influenced by the nature of the adhesive (*i.e.* mechanical properties, chemical formulations, fillers, *etc.*): even though both adhesives A and B are bicomponent epoxy adhesives, the pores in the adhesive B are more prone to changes that those in adhesive A. These changes being mainly growth and coalescence, it is plausible that they may contribute to premature failure mechanisms.

It is also important to investigate the influence of the spatial localisation of the pores on their sphericity. In a first stage, the influence of the position in the (xy) plane is studied (see in Figure 12 for the plane definition), as presented in Figure 16. Only the data for the initial state ($F = 0\,N$) are displayed, since they are sufficient to analyse the influence of this factor.

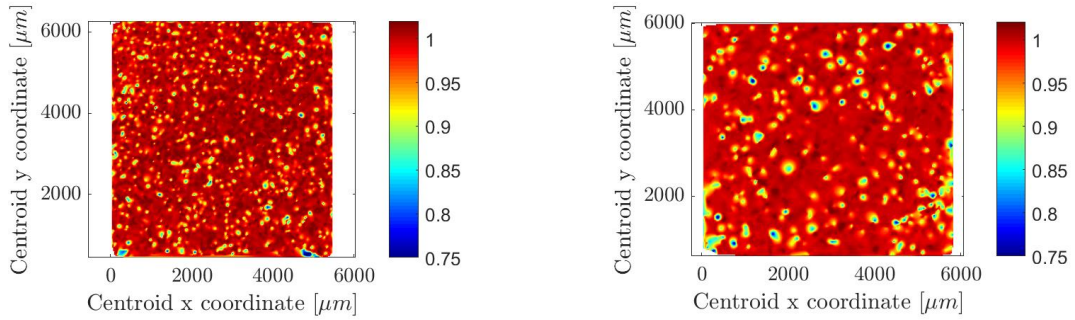

(a) Adhesive A (b) Adhesive B

Figure 16: Sphericity maps with respect to the coordinates along $\vec{x}$ and $\vec{y}$

No significant influence of the coordinates along $\vec{x}$ and $\vec{y}$ can be evidenced so far, regardless the adhesive. In particular, it seems that the proximity of the edges of the substrates does not impact the roundness of the pores. However, due to the significant decrease in sphericity caused by merged pores, it is rather difficult to extract a trend for the variation of Ψ with respect to the localisation in the plane of the adhesive joint. This trend is expected to be undetectable on the sphericity maps in Figure 16. Another convenient way to study this effect is to consider the radial distance of the pores with respect to the central axis of the adhesive joint (collinear with the $\vec{z}$ axis, Figure 12). This radial distance is computed using Equation 3.

$$\rho = \sqrt{(x - x_c)^2 + (y - y_c)^2}$$

Equation 3

where x and y are the coordinates of the centre of a given pore, and x_c and y_c are the coordinates of the centre of the joint.

Such an approach allows for a better visualisation of the effect of the pore localisation on its shape, even though it is downgraded to a 1D quantity where Figure 16 featured a 2D mapping. The corresponding results are plotted in Figure 17, for the initial load and the final load.

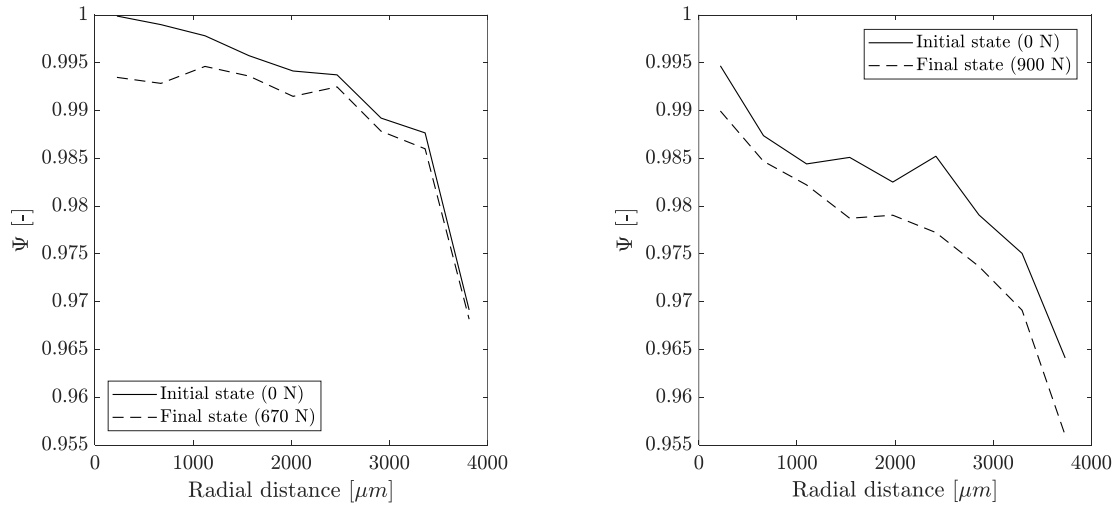

(a) Adhesive A (b) Adhesive B

Figure 17: Effect of the radial distance on the sphericity of the pores

The data in Figure 17a and Figure 17b show a fairly interesting trend, which was somehow overlooked in the sphericity maps in Figure 16. For both the studied adhesives, it seems that the roundness of the pores decreases with the radial distance to the centre of the joint. This could be explained by an effect of the surrounding material being different depending on the position within the joint (*i.e.* a confinement effect more homogeneous for a pore near the centre than for a pore close to the edges). Moreover, the decrease in sphericity caused by the application of a mechanical stress can also be seen in these curves, similarly to Figure 15c and Figure 15d. Nonetheless, an additional aspect is brought to light in Figure 17: the decrease seems to be more localised in the centre of the joint for the adhesive A, while it is more homogeneously distributed for the adhesive B. One may even notice a seemingly more intense decrease near the edges (radial distance above 2500 µm, Figure 17b). One may argue that it is a manifestation of the transversal strains caused by the tensile stress on the adhesive. This explanation could be supported by the fact that the Poisson ratios of the two adhesives are different (Table 1), that of the adhesive B being greater than that of the adhesive A. Therefore, the subsequent transversal strains being greater, the Poisson effect would explain the difference in behaviour for the considered adhesives.

Similar considerations can be made for the position of the pores centroids along $\vec{z}$, displayed in Figure 18.

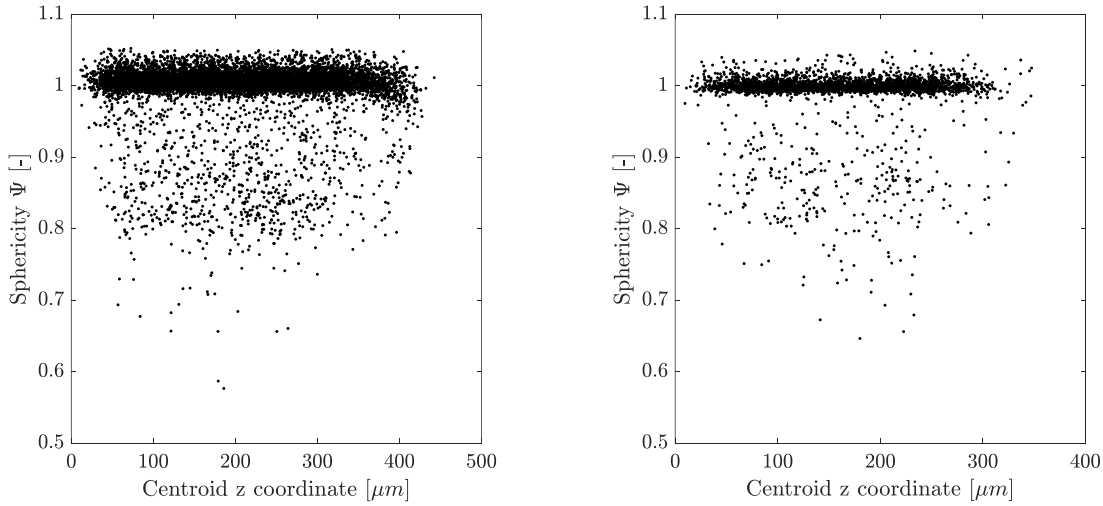

(a) Adhesive A (b) Adhesive B

Figure 18: Sphericities fluctuations along $\vec{z}$

The pores featuring the lowest sphericities tend to be located near the middle of the adhesive joint following $\vec{z}$, for both the adhesive A and the adhesive B. This could be explained by the fact that they are larger and more numerous in these parts, as shown later in this study. These characteristics are prone to induce segmentation errors for agglutinated pores, which are sometimes incorrectly merged into one unique binarised connected component during the segmentation. An example of such defects may be found in Figure 19. It is also possible to encounter actually merged pores, which probably coalesced during the curing. It is also clear that these coalescence phenomena are more likely to happen in the areas where the pores are bigger and more plentiful.

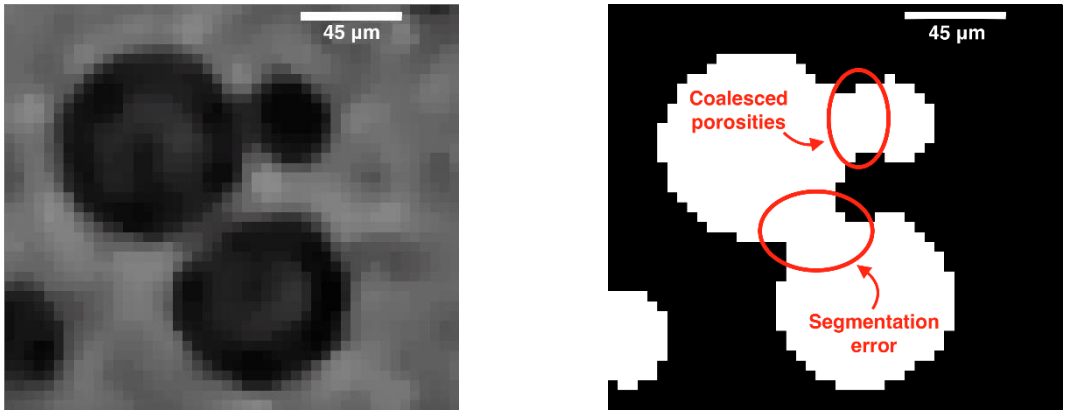

(a) Raw tomography data (b) Segmented pores (white pixels)

Figure 19: Segmentation defects and coalescence inducing low sphericity values (adhesive B, halfway through the joint thickness)

4.4. Effective section

The effective section is defined in Equation 4 as the ratio between the surface of adhesive $S_{adh}^{F_k}$ and the surface of joint ($\sum_{i \in phases} S_i^{F_k}$). Each quantity in Equation 4 exists for all the applied loads F_k, resulting in the following expression for the effective section $\Sigma_{eff}^{F_k}$.

$$\Sigma_{eff}^{F_k} = \frac{S_{adh}^{F_k}}{\sum_{i \in phases} S_i^{F_k}}$$

Equation 4

This quantity can be computed for each reconstructed slice along the $\vec{z}$ axis (see Figure 12 for the $\vec{z}$ axis definition). It provides information about the concentration zones of pores along this axis, which is also the loading direction. Moreover, by computing Σ_{eff} for various mechanical loads, it is possible to monitor the evolution of these concentration zones within the thickness of the adhesive joint. Figure 20 displays these evolutions for both adhesives A and B.

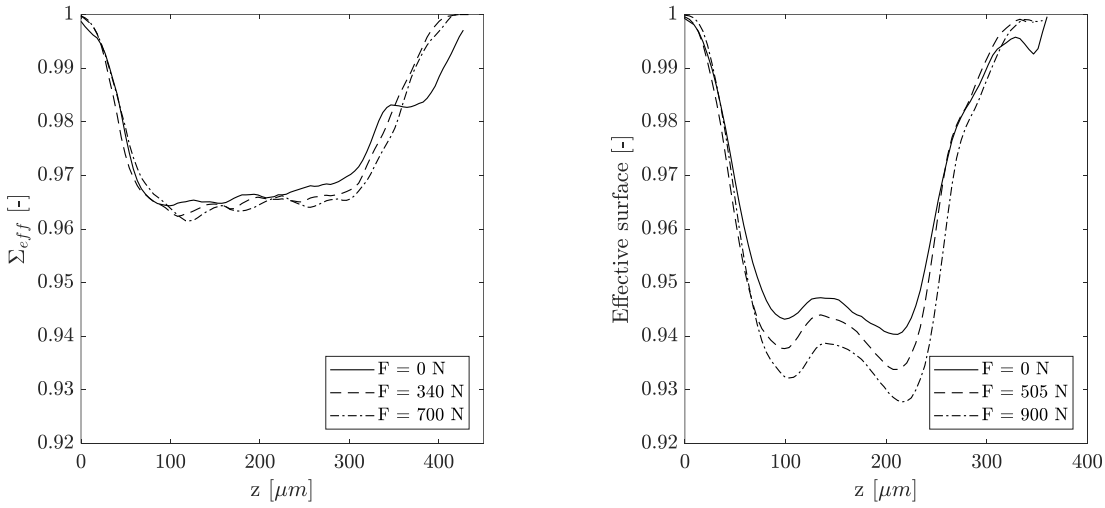

(a) Adhesive A (b) Adhesive B

Figure 20: Evolution of the effective sections Σ_{eff} of adhesive joints under tensile mechanical loadings

Both of the investigated adhesives feature lower effective sections approximately halfway through the thickness of the joint. This is explained by the fact that the largest pores tend to be located in the middle of the joint, as demonstrated by Figure 21. The pores tend also to be more numerous in this region (Figure 22). Furthermore, the application of a tensile loading accentuates this trend (dashed curves in Figure 20a and Figure 20b).

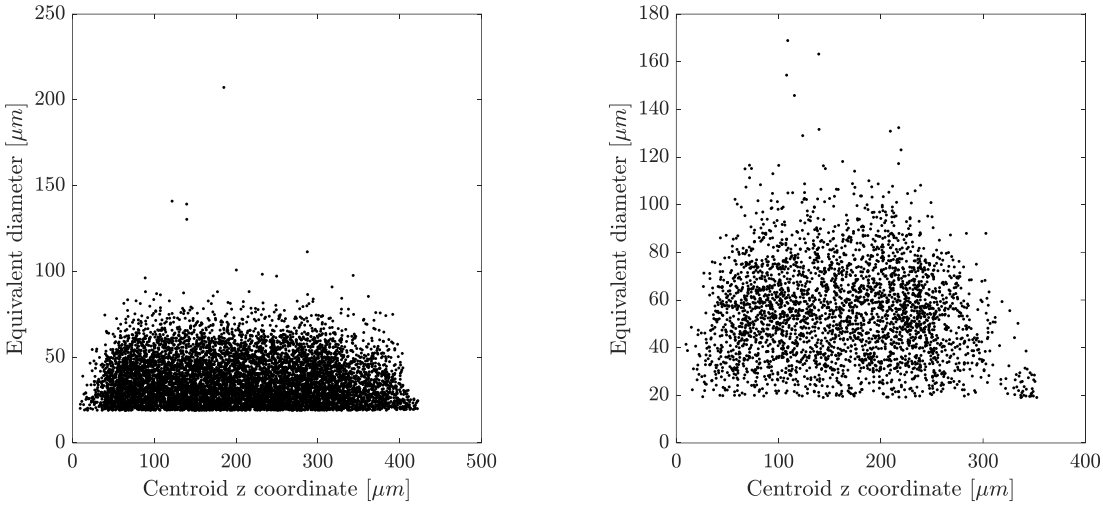

(a) Adhesive A (b) Adhesive B

Figure 21: Equivalent diameters of the pores plotted versus their location along $\vec{z}$ (initial states only)

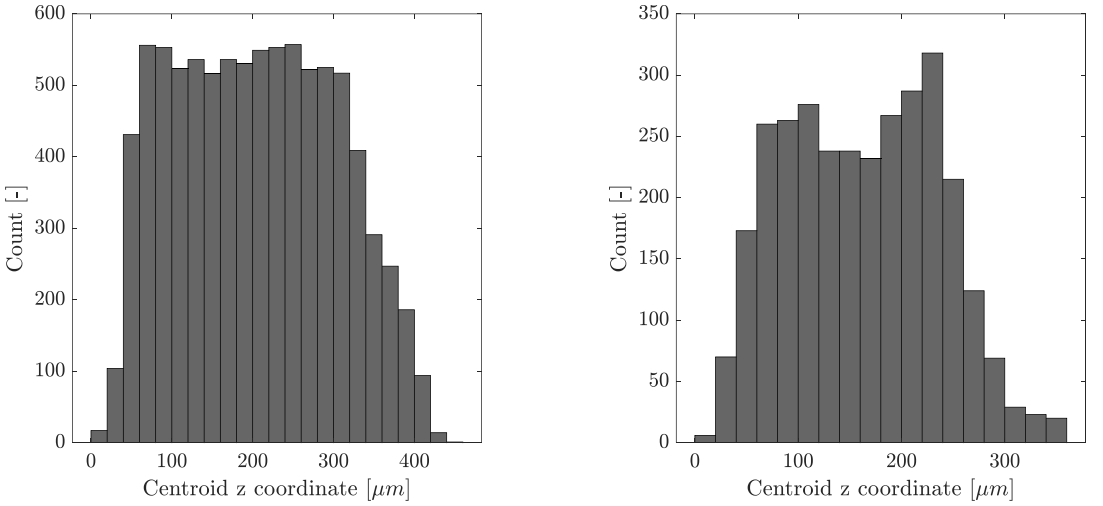

(a) Adhesive A (b) Adhesive B

Figure 22: Distributions of the pores centroids $\vec{z}$ coordinates

Several possible explanations of this phenomenon can be expressed. Due to the applied tensile loading, the Poisson effect along the $\vec{x}$ and $\vec{y}$, coupled with the expansion of the pores along $\vec{z}$ (suggested by the modification of their sphericities, Figure 15), could contribute to the reduction of the effective section.

Moreover, as shown in Figure 10 and Figure 11, the application of the tensile load tends to nucleate new pores (which may or may not coalesce afterwards), resulting in an increasing porosity ratio. It is therefore a similar observation that is made in Figure 20, except that instead of being volumetric quantities (such as the porosity ratio, see Equation 1), it is merely planar (surfaces in Equation 4).

One may notice that rather low values of Σ_{eff} are reached in the case of the adhesive B ($\Sigma_{eff} \sim 0.93$ in the worst case). An impact on the mechanical strength of the assembly could be expected from these low Σ_{eff}, especially due to the fact that the higher the load, the more Σ_{eff} decreases. Even in the scope of an approximate dimensioning, based on average stresses in the adhesive joint, the effect of

such a decrease in the effective section is easily evidenced. In the case of the adhesive B, the application of a 900 N load on a 36 mm^2 bonded surface results in an average stress of σ = 25 MPa. However, by taking into account this reduction in terms of effective surface, the average stress rises to σ = 27 MPa, *i.e.* an 8% increase. In addition to this point, the stress concentrations induced by the presence of pores suggests that, depending on their characteristics (size, relative spacing, *etc.*), their impact on the mechanical behaviour (in the context of both the strength of materials theory and the fracture mechanics theory) could be significant, such as premature failures due to unexpected stress concentrations in a low effective section zone of the bond.

5. Conclusion

Samples were bonded using structural epoxy adhesives in order to perform *in-situ* microtomography measurements under mechanical loads. Two adhesives were studied under out-of-plane tensile loadings, to investigate the influence of the applied load on the pores inside the joint. Using a specially designed segmentation tool, the tomography reconstructed volumes were segmented into their different constitutive phases. The isolated pores were firstly characterised using global quantities over the whole joint, such as their number and their volumetric fraction. It was shown that, depending on the adhesive, the evidenced phenomena were different: in both cases the tensile load induce the nucleation of new pores, but coalescence was experienced for only one of the materials. At this stage of the study, no particular explanation of this variation in behaviour can be brought into light.

The geometrical properties of the created pores were also studied. The distributions of their equivalent diameters showed different characteristics from one adhesive to another, and the impact of the tensile loading on these distributions was also quantified. Moreover, the computation of their sphericity demonstrated that the pores tend to deform from quasi-spherical into ellipsoidal entities.

Finally, the effective sections of the adhesive joints were calculated in all the investigated cases, resulting into two main conclusions. Firstly, the pores tend to be larger and more numerous halfway through the thickness of the adhesive bond, resulting in a fairly low effective section in this region of the joint. Secondly, this tendency is intensified by the application of a mechanical load, leading to even lower effective sections. This is an indicator of the threat that can be induced by the creation of pores in these materials. It can be easily understood that such structural defects can lead to stresses higher than expected, either due to precisely this decrease in effective section, or due to stress concentrations; and therefor trigger the premature mechanical failure of the assembly.

Another lead for future research worth to be mentioned is the possibility to perform a finer characterisation of the microstructure of such materials, either through X-ray microtomography with a higher resolution, or using other experimental techniques, such as N_2 sorption and Hg injection. Such experiments would provide interesting information regarding the minimal size of pores encountered in these materials, but significant difficulties are expected for them to be employed on assemblies. Therefore, at a first stage, a study on bulk samples would likely yield better results on this aspect.

References

[1] R. D. Adams, *Adhesive bonding: science, technology and applications*. Elsevier, 2005.

[2] O. Moussa, A. P. Vassilopoulos, and T. Keller, “Effects of low-temperature curing on physical behavior of cold-curing epoxy adhesives in bridge construction,” *Int. J. Adhes. Adhes.*, vol. 32, pp. 15–22, 2012, doi: 10.1016/j.ijadhadh.2011.09.001.

[3] J.-Y. Buffiere *et al.*, “In Situ Experiments with X ray Tomography: An Attractive Tool for Experimental Mechanics,” *Exp. Mech.*, vol. 50, pp. 289–305, 2010, doi: 10.1007/s11340-010-9333-7.

[4] X. Liu and C. Bathias, “Defects in squeeze-cast Al2O3/Al alloy composites and their effects on mechanical properties,” *Compos. Sci. Technol.*, vol. 46, no. 3, pp. 245–252, Jan. 1993, doi: 10.1016/0266-3538(93)90158-D.

[5] T. M. Breunig, S. R. Stock, A. Guvenilir, J. C. Elliott, P. Anderson, and G. R. Davis, “Damage in aligned-fibre SiC/Al quantified using a laboratory X-ray tomographic microscope,” *Composites*, vol. 24, no. 3, pp. 209–213, Jan. 1993, doi: 10.1016/0010-4361(93)90165-5.

[6] S. C. Garcea, Y. Wang, and P. J. Withers, “X-ray computed tomography of polymer

composites," *Compos. Sci. Technol.*, vol. 156, pp. 305–319, 2018, doi: 10.1016/j.compscitech.2017.10.023.
[7] J.-Y. Buffiere *et al.*, "Damage assessment in an Al/SiC composite during monotonic tensile tests using synchrotron X-ray microtomography," *Mater. Sci. Eng. A*, vol. 234–236, pp. 633–635, Aug. 1997, doi: 10.1016/S0921-5093(97)00302-X.
[8] J.-Y. Buffiere *et al.*, "Characterization of internal damage in a MMC-p using X-ray synchrotron phase contrast microtomography," *Acta Mater.*, vol. 47, no. 5, pp. 1613–1625, 1999.
[9] E. Maire *et al.*, "X-ray tomography applied to the characterization of cellular materials. Related finite element modeling problems," *Compos. Sci. Technol.*, vol. 63, no. 16, pp. 2431–2443, Dec. 2003, doi: 10.1016/S0266-3538(03)00276-8.
[10] E. Maire, V. Carmona, J. Courbon, and W. Ludwig, "Fast X-ray tomography and acoustic emission study of damage in metals during continuous tensile tests," *Acta Mater.*, vol. 55, no. 20, pp. 6806–6815, Dec. 2007, doi: 10.1016/j.actamat.2007.08.043.
[11] J. Adrien, E. Maire, N. Gimenez, and V. Sauvant-Moynot, "Experimental study of the compression behaviour of syntactic foams by in situ X-ray tomography," *Acta Mater.*, vol. 55, no. 5, pp. 1667–1679, Mar. 2007, doi: 10.1016/j.actamat.2006.10.027.
[12] M. Pavan, T. Craeghs, R. Verhelst, O. Ducatteeuw, J. P. Kruth, and W. Dewulf, "CT-based quality control of Laser Sintering of Polymers," *Case Stud. Nondestruct. Test. Eval.*, vol. 6, pp. 62–68, Nov. 2016, doi: 10.1016/j.csndt.2016.04.004.
[13] X. Wang, L. Zhao, J. Y. H. Fuh, and H. P. Lee, "Effect of porosity on mechanical properties of 3D printed polymers: Experiments and micromechanical modeling based on X-ray computed tomography analysis," *Polymers (Basel).*, vol. 11, no. 7, 2019, doi: 10.3390/polym11071154.
[14] M. Schwarzkopf and L. Muszynski, "Strain distribution and load transfer in the polymer-wood particle bond in wood plastic composites," *Holzforschung*, vol. 69, no. 1, pp. 53–60, 2015, doi: 10.1515/hf-2013-0243.
[15] P. E. McKinley, D. J. Ching, F. A. Kamke, M. Zauner, and X. Xiao, "Micro X-ray Computed Tomography of Adhesive Bonds in Wood," *Wood Fiber Sci.*, vol. 48, no. May, pp. 2–16, 2016.
[16] T. Rohr, S. Knaus, H. Gruber, and D. C. Sherrington, "Preparation and Porosity Characterization of Highly Cross-Linked Polymer Resins Derived from Multifunctional (Meth)acrylate Monomers," *Macromolecules*, 2002, doi: 10.1021/ma0110958.
[17] A. C. Kak and M. Slaney, *Principles of Computerized Tomographic Imaging*, *Society of Industrial and Applied Mathematics*. IEEE Press, 2001.
[18] B. Pollak, "Experiences with planography from the Fort William Sanatorium, Fort William, Ontario, Canada," *Dis. Chest*, vol. 24, no. 6, pp. 663–669, 1953.
[19] M. Sezgin, "Survey over image thresholding techniques and quantitative performance evaluation," *J. Electron. Imaging*, vol. 13, no. 1, pp. 146–165, 2004, doi: 10.1117/1.1631316.
[20] S. Beucher and F. Meyer, *Mathematical Morphology in Image Processing*, Marcel Dek. 1993.
[21] C. L. Lin, A. R. Videla, Q. Yu, and J. D. Miller, "Characterization and analysis of Porous, Brittle solid structures by X-ray micro computed tomography," *JOM*, vol. 62, no. 12, pp. 86–89, 2010.
[22] L. Grady, "Random Walks for Image Segmentation," *IEEE Trans. Pattern Anal. Mach. Intell.*, vol. 28, no. 11, pp. 1768–1783, 2006.
[23] F. Spitzer, *Principles of the Random Walk*. Princeton University Press, 1964.
[24] N. Otsu, "A Threshold Selection Method from Gray-Level Histograms," *IEEE Trans. Syst. Man. Cybern.*, vol. 9, no. 1, pp. 62–66, 1979, doi: 10.1109/TSMC.1979.4310076.
[25] N. C. Gallagher and G. L. Wise, "A Theoretical Analysis of the Properties of Median Filters," *IEEE Trans. Acoust.*, vol. 29, no. 6, pp. 1136–1141, 1981, doi: 10.1109/TASSP.1981.1163708.
[26] J. Koplik and A. Needleman, "Void growth and coalescence in porous plastic solid," *Int. J. Solids Struct.*, vol. 24, no. 8, pp. 835–853, 1988, doi: 10.1016/0020-7683(88)90051-0.
[27] B. R. Pinzer, A. Medebach, H. J. Limbach, C. Dubois, M. Stampanoni, and M. Schneebeli, "3D-characterization of three-phase systems using X-ray tomography: tracking the microstructural evolution in ice cream," *Soft Matter*, vol. 8, no. 17, p. 4584, 2012, doi: 10.1039/c2sm00034b.
[28] C. Landron, O. Bouaziz, E. Maire, and J. Adrien, "Experimental investigation of void

coalescence in a dual phase steel using X-ray tomography," *Acta Mater.*, vol. 61, no. 18, pp. 6821–6829, Oct. 2013, doi: 10.1016/j.actamat.2013.07.058.

[29] H. Wadell, "Volume, shape and roundness of quartz particles," *J. Geol.*, vol. 43, no. 3, pp. 250–280, 1935.

[30] G. Lehmann, D. Legland, and U. M. R. Génie, "Efficient N-Dimensional surface estimation using Crofton formula and run-length encoding," *Insight J.*, vol. 2, pp. 1–11, 2012.